# Aerodynamic Characteristics of a Family of Cone-Cylinder-Flare Projectiles

James E. Danberg,* Asher Sigal,† and Ilmars Celmins‡
*U.S. Army Ballistic Research Laboratory,*
*Aberdeen Proving Ground, Maryland*

**A systematic study of a number of flare-stabilized projectile geometries has been undertaken at the U.S. Army Ballistic Research Laboratory (BRL). Ten projectile configurations having identical forebodies and a variety of flares were tested in the BRL Aerodynamics Ballistic Range, and the results were compared to numerical computations based on two design codes and a parabolized Navier-Stokes (PNS) code. The design codes, in general, gave good results. The PNS code complimented these results by providing more details on the development of the aerodynamic forces. The results show the drag and stability tradeoffs involved for the different configurations. This information can be used to tailor the flare geometry to meet future mission requirements.**

## Nomenclature

$A$ = lateral surface area
$b$ = span of the fin or strake
$C_D$ = drag coefficient
$C_L$ = lift coefficient
$C_M$ = pitching moment coefficient
$C_N$ = normal-force coefficient
$C_p$ = pressure coefficient
$D$ = projectile diameter
$D_b$ = base diameter
$D_e$ = equivalent axisymmetric body diameter
$d$ = width of a side of a square body
$M$ = Mach number
$S$ = local, cross-sectional area of actual body
$S_R$ = reference area, $(\pi D^2/4)$
$X$ = axial distance from nose
$X_{CP}$ = location of the center of pressure
$\alpha$ = angle of attack

*Subscripts*

$b$ = base
$e$ = equivalent slender body
0 = zero lift conditions
$\infty$ = conditions at infinity

## Introduction

FLARE-STABILIZED projectiles are currently being evaluated for a variety of applications, including a 25-mm training round.[1] A systematic study of a number of flare geometries has been undertaken at the U.S. Army Ballistic Research Laboratory (BRL). The ultimate objectives of the study are 1) to determine how to increase the stability of a flare-stabilized round with a minimum increase in drag, and 2) to provide a range of aerodynamic data with which to determine the capabilities and limitations of available numerical predictive techniques.

Received May 26, 1989; presented as Paper 89-3371 at the AIAA Atmospheric Flight Mechanics Conference, Boston, MA, Aug. 14-16, 1989; revision received Oct. 2, 1989. 

*Aerospace Engineer. Associate Fellow AIAA.
†National Research Council Associate and Associate Professor of Aeronautics, Technion, Israel. Member AIAA.
‡Aerospace Engineer.

## Configurations

Ten projectile configurations are considered in this investigation, all with basically the same slightly blunted cone-cylinder forebody of almost 12 calibers. The projectile afterbody consists of a stabilizing flare, the angle and length of which were varied to provide a range of flare shapes. Figure 1 shows the overall geometry of the projectile with one of the flares (CS-V4-1) attached. A projectile of this design is smaller in diameter than the bore of the gun and thus must be enclosed in a sabot during launch. The cylindrical centerbody is grooved (buttress grooves) with matching threads on the sabot so that the loads created by the propellant can be transmitted from the sabot to the projectile.

Figure 2 shows all of the flare geometries. The CS-V1 configuration is a simple 15.2-deg half-angle, 2.67-caliber long flare (i.e., flare fineness ratio of 2.67 cylindrical center body diameters). The CS-V2 design has a 4-deg, 4.5-caliber flare. The CS-V4 family of flares are all basically derived from a 6-deg, 3.5-caliber baseline flare configuration. Configuration CS-V4-1 is the baseline flare. Configurations CS-V4-2 through CS-V4-5 consist of the baseline flare with one-caliber extensions of 6, 0, 12, and $-6$ deg, respectively.

Additionally, there are three other configurations in the CS-V4 group that are not simple conic or biconic shapes. CS-V4-7 has a $-6$-deg boattail, similar to CS-V4-5, but it also has a set of four fins with a 12-deg sweep angle located on the boattail. Configuration CS-V4-8 consists of the baseline configuration with four strakes extending along the length of the flare.

**Table 1 Geometrical parameters of the CS family of projectiles**

| Configuration | Flare fineness ratio | Flare angles | Base diameter ratio | Max. span ratio | Extension one caliber |
|---|---|---|---|---|---|
| CS-V1 | 2.67 | 15.20 | 2.450 | — | None |
| CS-V2 | 4.50 | 4.00 | 1.628 | — | None |
| CS-V4-1 | 3.50 | 6.00 | 1.736 | — | None |
| CS-V4-2 | 4.50 | 6.00 | 1.948 | — | 6-deg flare |
| CS-V4-3 | 4.50 | 6.00 | 1.736 | — | Cyl. skirt |
| CS-V4-4 | 4.50 | 6.00 | 2.160 | — | 12-deg biconic |
| CS-V4-5 | 4.50 | 6.00 | 1.526 | — | −6 deg boattail |
| CS-V4-6 | 4.50 | 9.53 | 1.540 | — | Square base |
| CS-V4-7 | 4.50 | 6.00 | 1.226 | 2.160 | Boattail with fins |
| CS-V4-8 | 3.50 | 6.00 | 1.736 | 2.043 | None |

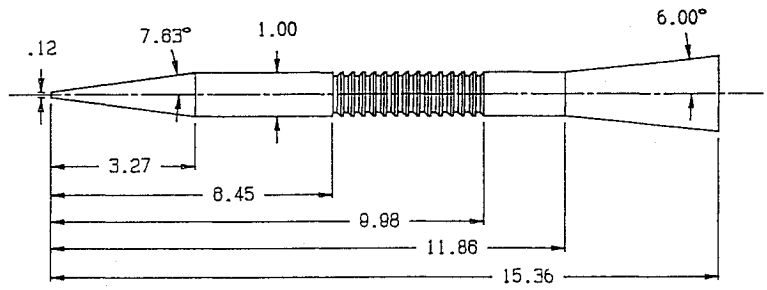


**Fig. 1 Sketch of baseline projectile with CS-V4-1 flare afterbody.**

Finally, configuration CS-V4-6 has a nonconical square base. The geometry of this shape was chosen so that the base area would be identical to that of the CS-V4-1 baseline, and so that the last caliber of length would have a square cross section. This dictates a flare angle of 9.53 deg.

Note that the basic shape corresponds to that of antiarmor projectiles of relatively large length-to-diameter ratio (about 16.3) where the center of gravity is near the mid-length. To maintain the same weight distribution, the projectile bodies were made of steel and the afterbodies were made of aluminum with an open cavity in the base.

The designations of the 10 flares and flare-fin stabilizers and their major geometrical relationships are given in Table 1.

## Experiment

A series of test firings have been carried out in the BRL Aerodynamics Range.[2] Up to five rounds of the CS-V1 and -V2 projectiles were fired at a number of fixed conditions from transonic to 4.6 in Mach number. Four rounds of each of the CS-V4 flare configurations were fired at a nominal Mach number of 4.0. The sabots used to launch the projectiles incorporated a slip-band obturator, which is designed to keep the roll rate at approximately one turn in 4 m of travel. Thus, the specific spin rate depends on launch velocity. Orthogonal spark shadowgraph pictures (see Fig. 3 for a typical picture) at stations along the range are interpreted to provide position and orientation throughout the flight. These data are fitted to the linearized equations of motion.[3] The fitting provides the linearized aerodynamic coefficient of drag and the slopes of the coefficient of moment and lift vs angle of attack. Center of pressure is determined from lift and pitching moment.

Additional information concerning the experiments, including tabulated experimental data, can be found in the reports of Celmins.[1,4]

## Design Code Analysis

Two kinds of predictive techniques have been applied to the family of configurations: fast turnaround design codes, which are ideally suited to parametric studies; and the parabolized Navier-Stokes (PNS) technique for solving the supersonic, thin shear-layer equations of motion.

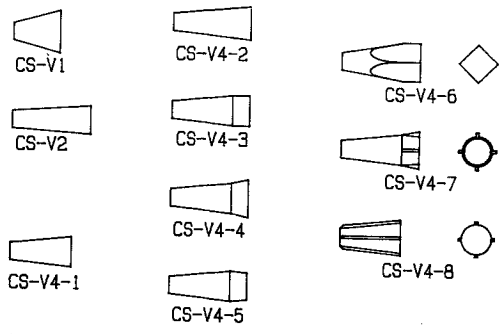


**Fig. 2 Afterbody and extension configurations.**

The missile DATCOM[5] and the Naval Surface Weapons Center (NSWC) aeroprediction[6] codes are capable of analyzing the aerodynamic characteristics of the proposed configurations. The two codes use the same methods for the evaluation of the inviscid contribution to the aerodynamic coefficients at supersonic speeds. In the present application, the Syvertson and Dennis second-order shock expansion (SOSE) method[7] was used. Both codes yield practically the same results for the normal-force and pitching-moment coefficients at small angles of attack and the same zero-lift wave-drag coefficients.

In the transonic region, the codes use data bases for the evaluation of the normal-force and the pitching-moment coefficients. The accuracy of the two data bases was evaluated by comparing predictions with the experimental data of Barth.[8] The slope of the normal-force curve and location of the center of pressure predicted by the DATCOM code were found in excellent agreement with the experimental data base. The NSWC code-predicted slopes were 11-27% lower than the experimental values. These findings concerning the NSWC code are consistent with previous conclusions of Sigal.[9] Therefore, it was decided to use the DATCOM code for the evaluation of the aerodynamic coefficients in the pitch plane. The pitch-plane coefficients were computed assuming an extended conical nose rather than the actual blunt nose. Corrections

**Table 2 Equivalent afterbody diameters**

| Configuration | $D_e/D$ | |
|---|---|---|
| | $X/D = 15.65$ | $X/D = 16.65$ |
| CS-V4-6 | 1.900 | 1.900 |
| CS-V4-7 | 1.736 | 1.870 |
| CS-V4-8 | 1.826 | — |

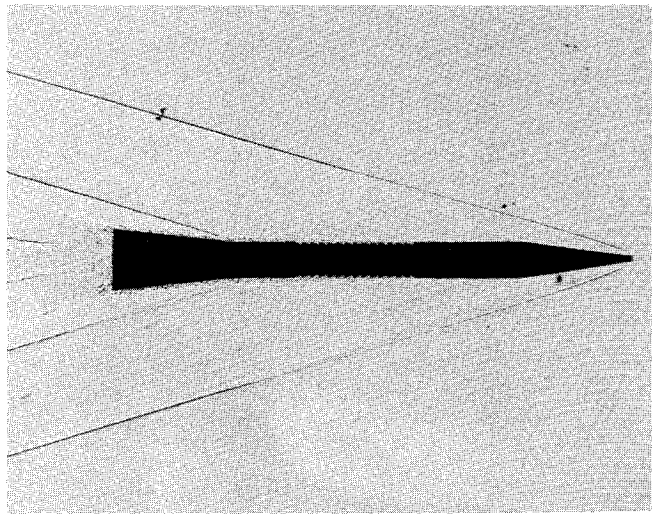

**Fig. 3 Spark shadowgraph of CS-V4-1 baseline projectile in flight (low yaw).**

were then applied to the normal-force and center-of-pressure locations. The systematic data base of Owens[10] for spherically blunted 10-deg cones was used in determining the correction. The estimate of the effects of truncation on the axial-force coefficient is based on the data of Esch[11] for truncated ogives since no data for truncated cones were found.

The two codes use different empirical methodologies for the estimation of the viscous contributions to the axial force coefficient. Since the outputs are different, these contributions were compared with the empirical data reported by Stoney.[12] It was found that the DATCOM code overpredicts the base drag coefficent of bodies having flares. The NSWC-aeroprediction code provides reliable prediction of the base drag coefficient for cylindrical and flared bodies. It uses an empirical data base for the estimation of the skin-friction coefficient in a wide range of Reynolds numbers, including the region of transition. This capability is of importance in the present case since the small projectile flies, most of the time, in the transition zone. The NSWC code was selected for the evaluation of the axial-force coefficient. Neither the NSWC nor the DATCOM codes have the ability to account for the effects of the buttress grooves. The groove roughness drag has been computed separately and added to the NSWC smooth body drag prediction as will be discussed in one of the following sections.

## Noncircular Stabilizers

Three configurations feature noncircular stabilizers. Configuration CS-V4-6 has a square base and CS-V4-7 and -8 have lifting surfaces mounted on the flares. Neither feature can be handled by the design codes without modification. Hence, equivalent axisymmetric configurations were used as computational models in these cases. The equivalent axisymmetric configuration's cross-sectional area distribution provides the same normal-force curve slope distribution as that of the actual configurations evaluated by slender body theory.

Using a centerbody cross-sectional area as the reference area for the equivalent body, the preceding condition becomes

$$(SC_{N\alpha}/S_R)_e = (SC_{N\alpha}/S_R)_{\text{actual}} \tag{1}$$

Since the equivalent body is circular, slender-body theory gives

$$(SC_{N\alpha}/S_R)_e = 2(D_e/D)^2 \tag{2}$$

For a slender body having a square cross section of dimension $d$ on a side, Nielsen[13] gives

$$SC_{N\alpha}/S_R = 2.4d^2/S_R = 3.056(d/D)^2 \tag{3}$$

Hence, for a square afterbody

$$D_e/D = 1.236(d/D) \tag{4}$$

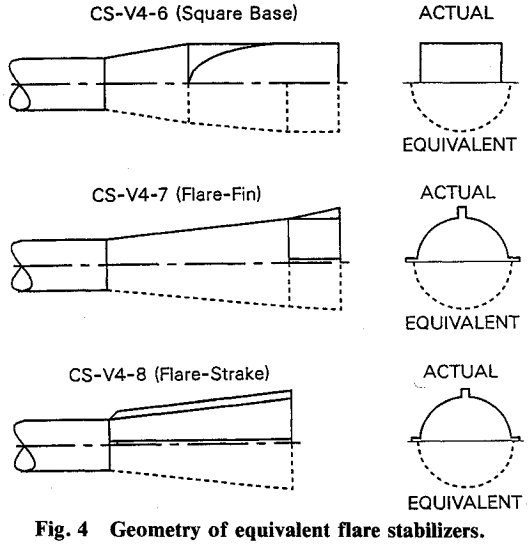


**Fig. 4 Geometry of equivalent flare stabilizers.**

For a cruciform slender wing-body combination, the same reference gives

$$SC_{N\alpha}/S_R = 2(b/D)^2[1 - (D_b/b)^2 + (D_b/b)^4] \tag{5}$$

so that

$$D_e/D = (b/D)[1 - (D_b/b)^2 + (D_b/b)^4]^{1/2} \tag{6}$$

The main geometrical parameters for the equivalent afterbodies are given in Table 2. A graphical comparison between the equivalent and the actual afterbodies is shown in Fig. 4.

## Buttress Groove Drag

This contribution to the axial-force coefficient is not included in the design codes. It is evaluated using the method of equivalent sand roughness and a new correlation for two-dimensional, ridge-type, roughness elements compiled by Sigal.[9] The ratio of the equivalent sand roughness to the height of the buttress grooves is estimated to be 2.0. The amplification in the skin-friction due to the roughness is evaluated using a friction law also compiled in Ref. 14.

## PNS Code

The flow over these configurations also has been computed using the PNS technique based on the code developed by Schiff and Steger.[15] This technique consists of generalized body-fitted coordinates, thin shear-layer, linearized, approximately factored equations. A finite-difference algorithm is solved implicitly using a block diagonal method as formulated by Beam and Warming.[16] The approximation, which permits marching in the primary flow direction, limits the application to attached, supersonic freestream flows. Thus, the results from the PNS code cannot provide information on the separated flow in the near wake or the base pressure. The base drag was estimated based on the method developed by Mueller et al.[17]

The code uses the Baldwin-Lomax[18] algebraic turbulence model to compute skin friction forces. The flow is assumed to

**Table 3 Tabulated results for CS-V4 configurations at $M_\infty = 4$**

| CS-V4 | | $C_{D_0}$ | $C_{M_\alpha}$ | $C_{N_\alpha}$ | $X_{CP}/D$ | $X_{CG}/D$ |
|---|---|---|---|---|---|---|
| 1 | EDC[a] | 0.523 | −3.38 | 6.27 | 8.35 | 7.81 |
| | PNS[b] | 0.580 | −3.01 | 5.79 | 8.33 | |
| | EXP[c] | 0.532 | −6.40 | 6.27 | 8.83 | |
| 2 | EDC | 0.634 | −13.14 | 7.73 | 9.80 | 8.10 |
| | PNS | 0.686 | −11.46 | 7.03 | 9.73 | |
| | EXP | 0.646 | −15.02 | 7.59 | 10.08 | |
| 3 | EDC | 0.543 | −8.20 | 7.01 | 9.15 | 7.98 |
| | PNS | 0.578 | −4.38 | 6.08 | 8.70 | |
| | EXP | 0.542 | −8.17 | 6.86 | 9.17 | |
| 4 | EDC | 0.879 | −21.63 | 8.90 | 10.64 | 8.21 |
| | PNS | 0.940 | −24.30 | 8.68 | 11.01 | |
| | EXP | 0.849 | −25.07 | 9.22 | 10.93 | |
| 5 | EDC | 0.529 | −5.11 | 6.64 | 8.76 | 7.99 |
| | PNS | 0.539 | −1.02 | 5.68 | 8.17 | |
| | EXP | 0.504 | −3.48 | 6.33 | 8.54 | |
| 6 | EDC | 0.637 | −12.77 | 8.29 | 9.83 | 8.29 |
| | PNS | 0.663 | −10.55 | 7.43 | 9.71 | |
| | EXP | 0.607 | −13.08 | 8.19 | 9.88 | |
| 7 | EDC | 0.529 | −11.35 | 7.42 | 9.52 | 7.99 |
| | PNS | — | — | — | — | |
| | EXP | 0.530 | −8.13 | 6.78 | 9.19 | |
| 8 | EDC | 0.523 | −6.74 | 6.81 | 8.82 | 7.83 |
| | PNS | — | — | — | — | |
| | EXP | 0.571 | −11.87 | 7.46 | 9.42 | |

[a]EDC = Engineering design codes. [b]PNS = PNS code. [c]EXP = BRL aerodynamics range.

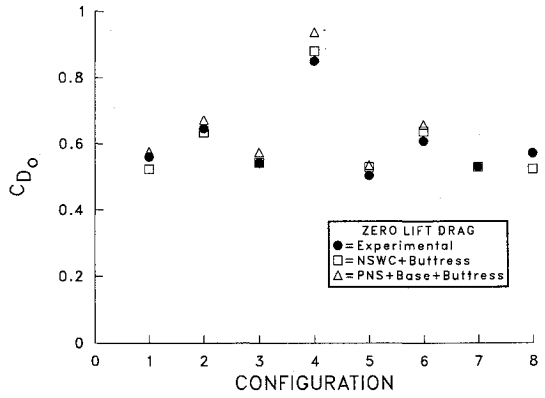


**Fig. 5 Zero-lift drag coefficient for CS-V4 configurations at $M_\infty = 4.0$.**

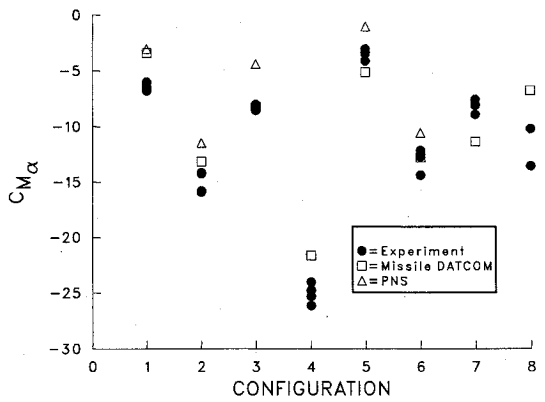


**Fig. 6 Slope of the pitching-moment coefficient about the center of gravity for CS-V4 configurations at $M_\infty = 4.0$.**

be turbulent from the nose although this may somewhat overestimate the actual viscous contribution. The same estimate of buttress groove drag that was used for the design codes was also applied to the PNS results.

In principle, the PNS code can handle all the nonconical shapes considered, including the fin and strake bodies, but these shapes have not been attempted here. PNS results are reported only for the axisymmetric shapes and the square base configuration.

## Results

### Effects of Afterbody Shape

The basic computed (design and PNS codes) and measured results of this project for the CS-V4 family of configurations at a flight Mach number of 4.0 are contained in Figs. 5–8. Typical tabulated data are given in Table 3. The figures show the individual experimental aerodynamic data obtained from the range tests. The fitted $C_{D_0}$ values of four rounds for each configuration are given in the table. The experimental normal force could be determined from only two of the four rounds for configurations 2, 3, 4, 6, and 8 because of low yaw. For the same reason, it was impossible to evaluate $C_{M\alpha}$ for one round from configurations 3 and 6 and two rounds from configuration 8.

Figure 5 shows the zero-lift drag coefficient for the eight CS-V4 configurations at a Mach number of 4.0 and a Reynolds number based on model cylinder diameter of $2.36 \times 10^6$. The baseline configuration (CS-V4-1) has a measured drag coefficient of 0.53. The lowest drag is obtained from the boattailed configuration ( − 5). This is not surprising since the boattail affects the base pressure, which in turn determines the major component of the drag. The largest drag is produced, as expected, by the biconic shape with its 12-deg flare and consequent high wave and base drag component.

The difference between the NSWC aeroprediction code predicted drag coefficient and the data is less than 0.02 for half the configurations. The corresponding value for the difference between the PNS results and the data is twice as large because turbulent flow was assumed from the tip.

Figure 6 shows the effect of the different configurations on the pitching moment about the center of gravity of the projectiles. The center of gravity varied only slightly between configurations, as can be seen in Table 3. The differences in moment are mainly, but not entirely, due to aerodynamic effects. Obviously, the two most stable configurations, ( − 2) and ( − 4), are also the configurations with the highest drag. Configuration ( − 6) has somewhat higher drag than the baseline, but it has much improved stability.

The predictive methods generally give a smaller negative pitching moment. The second-order shock expansion method of the missile DATCOM code consistently gives slightly better agreement with the experimental data than the PNS computation.

Figure 7 shows the lift coefficient slope, and Fig. 8 shows the center-of-pressure measured from the blunted nose of the projectiles. These two figures provide an alternative way of looking at the pitching-moment slope results. In general, the missile DATCOM code adequately predicts both the lift slope and the center of pressure, whereas the PNS code consistently underpredicts lift and center of pressure. It is possible that the DATCOM results are fortuitous, however, because the DATCOM code predicts the lift and center-of-pressure neglecting viscous effects. The smooth-body viscous effects are accounted for in the PNS code, and the afterbody lift is significantly less than predicted by the design code, resulting in the more forward center of pressure. However, the buttress grooves are not accounted for in the computations.

One possible explanation for both the DATCOM and the PNS codes underprediction of the stability (see Fig. 6) relative

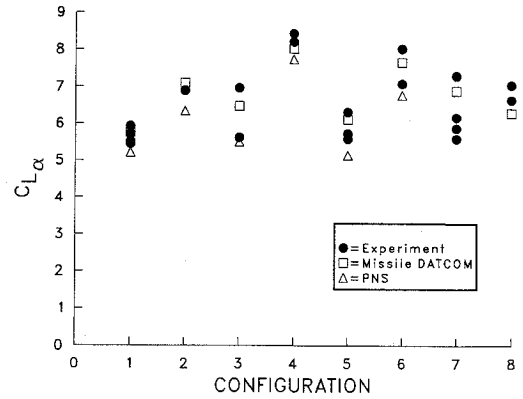


**Fig. 7 Slope of the lift coefficient for CS-V4 configurations at $M_\infty = 4.0$.**

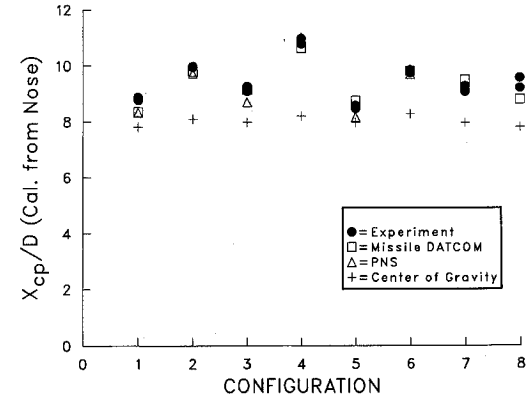


**Fig. 8 Center of pressure location from the projectile nose for CS-V4 configurations at $M_\infty = 4.0$.**

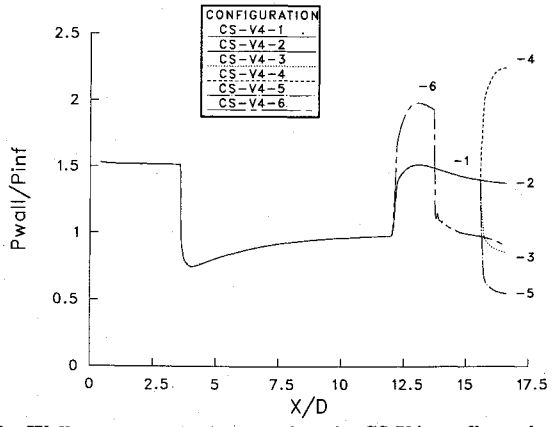


**Fig. 9 Wall pressure distribution for six CS-V4 configurations at $M_\infty = 4.0$, $\alpha = 1$ deg leeside.**

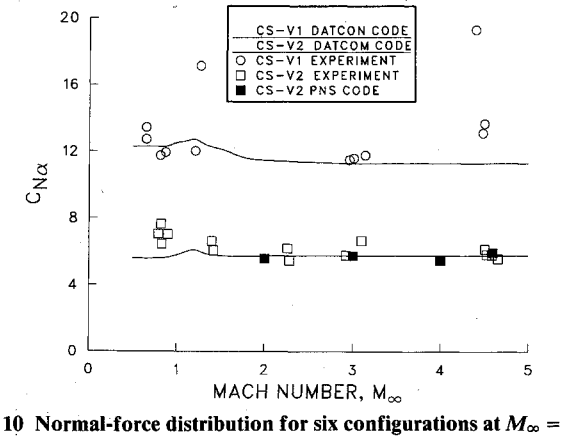


**Fig. 10 Normal-force distribution for six configurations at $M_\infty = 4.0$, $\alpha = 0$ deg.**

to the experimental data is that the enlarged boundary layer produced by the grooves is greatly distorted circumferentially at the angle of attack so that the lee-side flare becomes less effective relative to the wind side. Thus the flare lift is greater than predicted with a more rearward center of pressure. An alternate explanation for the lower afterbody lift in the computations, relative to the experiment, is that the cavity in the rear of the models is so large (over 4.0 calibers) that a small internal pressure difference between the top and bottom surfaces could produce a considerable lift with a sufficiently large moment arm to account for the observed discrepancies.

Although the DATCOM code matches the data fairly accurately, there are some discrepancies between predicted and observed data trends. As can be seen in Fig. 7, both the range data and the PNS code show that configuration CS-V4-5 (boattail) is less stable than configuration CS-V4-1 (baseline). The DATCOM results show CS-V4-5 to be more stable. This trend also exists for the lift coefficient slope and center-of-pressure location, although it is not as clearly visible. This reversal of the data trends can lead to serious problems when choosing a projectile geometry for a particular application, which is one function of a projectile design code.

### Pressure Distributions

One of the primary advantages of using the PNS code is the detail that can be obtained concerning the pressure and force distribution for the various shapes. Figure 9 shows the pressure distribution on the leeward side of the first six configurations at 1-deg angle of attack. Among the first five configurations, the effectiveness of decreasing the slope of the body on the last caliber is clearly evident. Configuration ( − 6) produces its higher stabilizing lift because of the larger flare angle (9.53 deg compared to the 6 deg of the others), and because of the transition to a square cross section the pressure drops to nearly the same level as the cylindrical skirt body.

### Normal Force Distribution

Figure 10 shows the distribution of the normal force in terms of the slope of the normal force as a function of $X/D$ for the five configurations. The nose is found to contribute 1.97 to the slope, which is 97% of the slender-body prediction. The cylindrical midbody contributes only about half of that of the nose at this Mach number, but computations show that it tends to provide an increasing contribution with Mach number. The 8.5-caliber cylinder is sufficiently long so that increasing its length would not provide significant additional lift. The 6-deg, 3.5-caliber flare contributes more lift than the entire forebody.

The effect of the normal force on the various 7-caliber extensions is important in terms of stability because this force acts over a large moment arm relative to the c.g. The 12-deg biconic ( − 4) substantially increases the normal force and stabilizing moment. As the angle of the extension is decreased ( − 2, − 3), the normal force also decreases, until for the boattailed extension ( − 5) the normal force is actually negative, thereby reducing the stabilizing moment.

### Drag Breakdown

Figure 11 shows the Mach number behavior of the smallest flare angle configuration (CS-V2) as well as the components of the drag. Both the modified design code and the PNS code predict the data within the scatter in the measurements above Mach 3. Below that point the scatter in the data becomes large, but with the NSWC code again underpredicting the data. The base drag, at speeds below about Mach 2, is equal to or greater than all the other contributors. The other factors remain surprisingly constant over the Mach number range considered here. The PNS code results are also indicated on the figure. The PNS code can only compute the pressure and friction

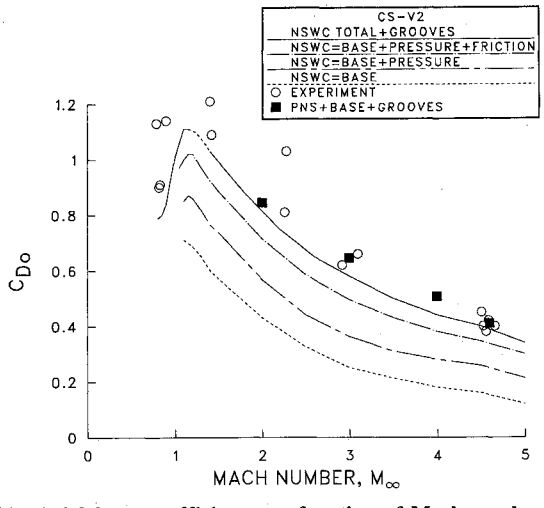


**Fig. 11 Axial-force coefficient as a function of Mach number with component breakdown for the CS-V2 configuration.**

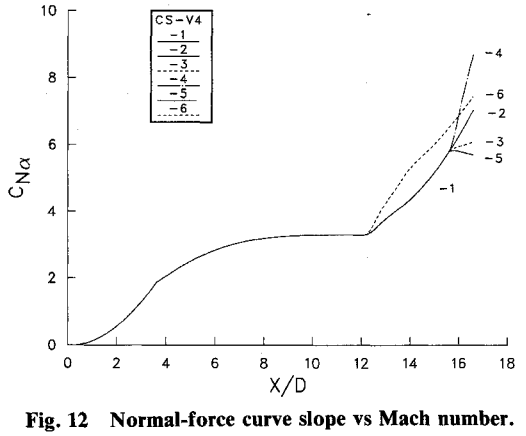


**Fig. 12 Normal-force curve slope vs Mach number.**

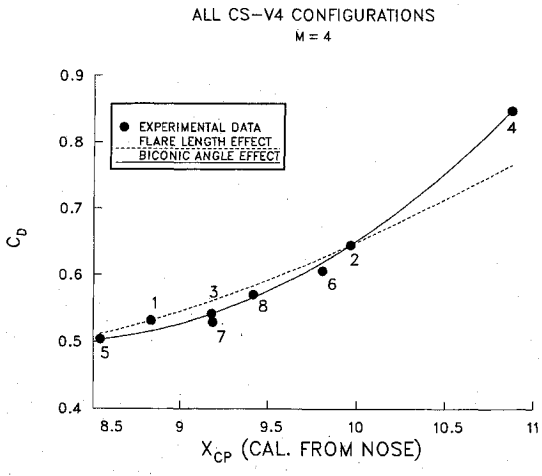


**Fig. 13 Correlation of drag coefficient with center-of-pressure location at $M_\infty = 4.0$.**

components of the drag. The base drag has been obtained from the correlations based on Mueller's technique. These calculations have been added to the PNS results as well as the buttress groove drag. These composite PNS results are in better agreement with the data than those of the design code. However, this is in part due to a higher skin friction drag predicted by the Navier-Stokes code. One reason for the larger friction drag is that turbulent flow was assumed from the start of the numerical computation whereas the design code incorporated an empirical transition.

#### Normal Force Slope

Figure 12 shows the Mach number dependence of the normal force. The experiments indicate, and both computational methods predict, that there is very little variation of the lift with supersonic Mach number. For the CS-V2 case, both the PNS and DATCOM codes predict the data with equal accuracy. The tendency for the CS-V1 experimental $C_{N_\alpha}$ to increase above $M_\infty = 4$ may not be valid because of the large scatter in those particular measurements.

#### Most Effective Configuration

Figure 13 presents the measured data as a correlation of drag coefficient with center-of-pressure location. This format is chosen to emphasize the tradeoffs between stability and drag. Stability is evaluated using the center of pressure in order to eliminate the effect of c.g. differences. The "best" configurations have the most rearward center of pressure and the least drag, and are thus located toward the bottom right corner of the figure. A single continuous curve can be drawn through the data of configurations ( − 1) and ( − 2) showing the effect of flare length for a single flare angle, i.e., increasing the flare length from 3.5 calibers [configuration ( − 1)] to 4.5 calibers [configuration ( − 2)] increases the drag coefficient by 0.11 and shifts the center of pressure back by 1.1 calibers. Configurations ( − 5), ( − 3), ( − 2), and ( − 4) also form a related series of afterbody shapes, starting with the boattail and ending with the 12-deg biconic body. A curve drawn through these four points shows the effect of the angle of a 1-caliber extension to the baseline flare. The figure shows that, for biconic flares, extensions with larger angles than the baseline flare are less efficient than simply extending the flare length. Conversely, extensions with a shallower flare angle are desirable. The square ( − 6) and fin ( − 7) configurations are judged the most effective for improving stability at a minimum penalty in drag. However, if flare length is a limiting factor, it should be noted that the addition of strakes ( − 8) to the 3.5-caliber baseline ( − 1) results in a substantial stability increase with no increase in length.

## Conclusions

Ten flare-stabilized projectile configurations have been tested in the BRL Aerodynamics Ballistic Range, and the results have been compared to numerical computations based on two design codes and a parabolized Navier-Stokes (PNS) code. The evaluation of the results show the following.

1) The configuration with a combination of 6-deg, flare boattail with small fins produced the most stable shape with the least drag penalty as compared to conventional flares.

2) The prediction of the aerodynamic characteristics using the NSWC aeroprediction code gave, in general, very good results, despite the fact that effective bodies had to be devised to represent the actual body shapes and that corrections had to be introduced to account for the buttress thread roughness effects. However, some of the data trends for biconic configurations were not predicted correctly.

3) The PNS results complemented the semiempirical computations by providing more detail on the development of the aerodynamic forces. The PNS pitching-moment prediction is consistently less than the measurements, possibly because of the effect of the open base cavities or of the buttress groove boundary layer on the projectiles tested.

## References

[1]Celmins, I., "Aerodynamic Characteristics of Fin- and Flare-Stabilized 25 mm Training Round Prototypes," *Proceedings of the 10th International Symposium on Ballistics,* Vol. 1, American Defence Preparedness Association, Arlington, VA, Oct. 1987; also, U.S. Army Ballistic Research Lab., Aberdeen Proving Ground, MD, BRL-TR-2882, Dec. 1987 (AD A191683).

[2]Braun, W. F., "The Free Flight Aerodynamic Range," U.S. Ballistic Research Lab., Aberdeen Proving Ground, MD, BRL Rept. 1048, Aug. 1958 (AD 202249).

[3]Murphy, C. H., "Data Reduction for the Free Flight Spark Ranges," U.S. Army Ballistic Research Lab., Aberdeen Proving Ground, MD, BRL Rept. 900, Feb. 1954 (AD 35833).

[4]Celmins, I., "Drag and Stability Tradeoffs for Flare-Stabilized Projectiles," U.S. Army Ballistics Research Lab., Aberdeen Proving Ground, MD (to be published).

[5]Vukelich, S. R., and Jenkins, J. E., "Missile DATCOM: Aerodynamic Prediction of Conventional Missiles Using Component Build-Up Techniques," AIAA Paper 84-0388, Jan. 1984.

[6]Mason, L. A., Devan, L., Moore, F. G., and McMillian, D., "Aerodynamic Design Manual for Tactical Missiles," Naval Surface Weapons Center, Dahlgren, VA, NSWC TR 81-156, 1981.

[7]Syvertson, C. A., and Dennis, D. H., "A Second-Order Shock Expansion Method Applicable to Bodies of Revolution near Zero-Lift," NACA Rept. 1328, 1957.

[8]Barth, H., "Data for Determining Normal-Force, Moment and Tangential-Force Characteristics of Nose-Cylinder Configurations in the Transonic Velocity Range," Messerschmitt-Bölkow-Blohm, GMBH, Schrobenhausen, FRG, MBB Rept. WE-2-97/69, 1969.

[9]Sigal, S., "A Critical Review of Data Bases on the Normal-Force and the Center-of-Pressure Location of Bodies," Technion, Israel, 1985, ARC Rept. 0-229 (in Hebrew).

[10]Owens, R. V., "Aerodynamic Characteristics of Spherically Blunted Cones at Mach Numbers from 0.5 to 5.0," NASA TN D-3088, 1965.

[11]Esch, H., "Bodies," *Missile Aerodynamics,* AGARD-LS-98, Article No. 4, 1979.

[12]Stoney, A., "Collection of Zero-Lift Drag Data," NASA TR Rept. 100, 1962.

[13]Nielsen, J. N., *Missile Aerodynamics*, McGraw-Hill, New York, 1960, Chap. 3.

[14]Danberg, J. E., and Sigal, A., "Analysis of Turbulent Boundary Layer over Rough Surfaces," U.S. Army Ballistic Research Lab., Aberdeen Proving Ground, MD, BRL-TR-2977, Dec. 1988 (AD 206747).

[15]Schiff, L. B., and Steger, J. L., "Numerical Simulation of Steady Supersonic Viscous Flow," AIAA Paper 79-0130, Jan. 1979.

[16] Beam, R., and Warming, R. F., "An Implicit Factored Scheme for the Compressible Navier-Stokes Equations," *AIAA Journal*, Vol. 16, No. 4, 1978, pp. 85–129.

[17]Mueller, T. J., Hall, C. R., Jr., and Roache, P. J., "The Influence of Initial Flow Direction on the Turbulent Base Pressure in Supersonic Axisymmetric Flow," AIAA Paper 70-555, May 1970.

[18]Baldwin, B. S., and Lomax, H., "Thin Layer Approximation and Algebraic Model for Separated Turbulent Flows," AIAA Paper 78-257, Jan. 1978.

Walter B. Sturek
*Associate Editor*